

# CHROMOSPHERIC DOWNFLOWS AS A DIAGNOSTIC OF SOLAR FLARE HEATING

DOMINIC M. ZARRO<sup>1</sup> and RICHARD C. CANFIELD<sup>2</sup>

<sup>1</sup>Applied Research Corporation, Landover, MD\*

<sup>2</sup>Institute for Astronomy, University of Hawaii, Honolulu, HI

## ABSTRACT

Using coordinated X-ray and H $\alpha$  observations of five solar flares, we investigate the dynamics of chromospheric condensations formed during chromospheric evaporation. We show that the peak downflow velocity of condensations predicted by simple hydrodynamic compression of the chromosphere is in good agreement with empirical downflow velocities implied by impulsive phase H $\alpha$  redwing Doppler shifts. This agreement indicates that the H $\alpha$  wing redshift provides a useful diagnostic of the pressure excess in the evaporating region and, hence, the energy flux driving chromospheric evaporation.

## I. INTRODUCTION

The chromospheric condensation formed during chromospheric evaporation consists of cool, dense plasma created by the passage of a radiating hydrodynamic shock (Fisher 1986). This condensation is a direct consequence of a momentum conserving backpressure exerted on the chromosphere during the flare heating phase. Fisher (1987) has shown that the peak downflow velocity  $v_d$  of chromospheric condensations is given by the relation

$$v_d = \sqrt{(P_2 - P_1)/\rho_c}, \quad (1)$$

where  $P_2$  is the pressure in the evaporating region, and  $P_1$  and  $\rho_c$  are preflare values of chromospheric pressure and density ahead of the initial location of the condensation front. For five flares observed simultaneously in H $\alpha$  at *Sacramento Peak Observatory* (SPO) and in X-rays with the *Solar Maximum Mission* (SMM), we have sufficient information to test quantitatively this relationship.

Each flare showed evidence for chromospheric evaporation in the form of simultaneous upflowing coronal X-ray plasma and downflowing chromospheric plasma during the impulsive phase (Canfield *et al.* 1988). Table 1 lists physical parameters derived for each flare using combined H $\alpha$  and X-ray observations. Further details of these observations are given in the references cited in Table 1.

## II. DATA REDUCTION

The SPO H $\alpha$  observations consist of spectra with 0.1 Å resolution over a 10 Å range, and spectroheliograms with  $\sim 2.6$  arcsec<sup>2</sup> pixel resolution in a 2–3 arcmin field of view. Each pixel was sampled with a repetition period of between 15 and 25 s. For each pixel, we derive a flare profile by subtracting a reference preflare profile obtained in that pixel immediately before the start of impulsive hard X-rays. Almost all flaring pixels show red H $\alpha$  asymmetry (excess red emission), while only a few show blue asymmetry. Figure 1 shows the typical temporal variation of flare profiles in one of the pixels of the 23 June 1980 event.

For each flare pixel, we determine the peak condensation velocity from the maximum redshift of the H $\alpha$  wing centroid observed during the impulsive phase. From the total number of pixels showing redshifts, we compute a total chromospheric downflow area  $S_c$ , and a characteristic maximum downflow velocity  $v_{max}$  averaged over this area. For each flare, we identify footpoints of opposite magnetic polarity on the basis of coaligned H $\alpha$  spectroheliograms and magnetograms from *Kitt Peak National Observatory* (KPNO). Assuming that the footpoints are connected by a semi-circular coronal arch, we estimate characteristic loop half-lengths  $L \approx \pi D/4$ , where D is the footpoint separation.

\* under contract with Lockheed Palo Alto Research Laboratory.

TABLE 1  
PARAMETERS OF X-RAY AND II $\alpha$  ANALYSIS

|  | 7 May 1980<br>14:56 UT | 23 June 1980<br>23:12 UT | 24 June 1980<br>15:22 UT | 25 June 1980<br>15:52 UT | 30 April 1985<br>23:43 UT |
|--|------------------------|--------------------------|--------------------------|--------------------------|---------------------------|
| $T_0$ ( $10^6$ K)                            | 3.0                    | 3.4                      | 3.8                      | 3.4                      | 3.2                       |
| $P_0$ (dynes cm $^{-2}$ )                    | 20.                    | 23.                      | 37.                      | 17.                      | 14.                       |
| $L$ ( $10^8$ cm)                             | 5.7                    | 7.3                      | 6.5                      | 10.                      | 10.                       |
| $S_c$ ( $10^{17}$ cm $^2$ )                  | 1.1                    | 3.5                      | 4.5                      | 5.2                      | 4.0                       |
| $P_{20}$ ( $10^{28}$ ergs s $^{-1}$ )        | 6.7                    | 5.3                      | 5.0                      | 18.                      | 1.7                       |
| $\delta$                                     | 4.8                    | 7.0                      | 6.5                      | 6.3                      | 5.3                       |
| $N_{tr}$ ( $10^{19}$ cm $^{-2}$ )            | 1.4                    | 1.8                      | 2.3                      | 1.8                      | 1.6                       |
| $F'$ ( $10^{11}$ ergs cm $^{-2}$ s $^{-1}$ ) | 1.0                    | .45                      | .40                      | .98                      | .09                       |
| $P_2$ (dynes cm $^{-2}$ )                    | 1210                   | 704                      | 735                      | 1064                     | 210                       |
| $\rho_c$ ( $10^{-11}$ gm cm $^{-3}$ )        | 3.9                    | 4.7                      | 7.5                      | 3.5                      | 2.9                       |
| $v_{max}$ (km s $^{-1}$ )                    | 41 $\pm$ 8             | 42 $\pm$ 8               | 37 $\pm$ 12              | 24 $\pm$ 12              | 60 $\pm$ 10               |
| $v_d$ (km s $^{-1}$ )                        | 55                     | 38                       | 31                       | 55                       | 27                        |
| Ref. <sup>a</sup>                            | 1,2,3                  | 4                        | 2,5                      | 6                        | 7                         |

<sup>a</sup>REFERENCES.— (1) Acton *et al.* 1982. (2) Canfield, Gunkler, and Kiplinger 1984. (3) Canfield and Gunkler 1985. (4) Canfield *et al.* 1988. (5) Gunkler *et al.* 1984. (6) Kundu, Schmahl, and Velusamy 1982. (7) Zarro *et al.* 1988.

Prior to each flare, the Flat Crystal Spectrometer (FCS; 14 arcsec field of view) on the SMM X-ray Polychromator (XRP) imaged the associated preflare active region in the two soft X-ray O VIII (18.97 Å) and Mg XI (9.17 Å) lines. From the ratio of fluxes in these two optically thin lines (averaged over a 4 arcmin $^2$  field in each region), we calculate isothermal preflare coronal temperatures  $T_0$ . Substituting  $T_0$  and the II $\alpha$ -inferred loop lengths  $L$  into the scaling law for conduction-dominated coronal loops (Craig, McClymont, and Underwood 1978), we derive preflare coronal pressures  $P_0$  and densities  $n_0$ . Assuming pressure balance between the preflare corona and chromosphere, and a quiescent chromospheric temperature  $T_{ch} = 8000$  K, we infer preflare chromospheric densities  $\rho_c$ .

Hard X-ray observations during the impulsive phase of each event were obtained with the SMM Hard X-ray Burst Spectrometer (HXRBS). Applying a power-law fit to the hard X-ray photon spectrum and adopting a thick-target electron model for hard X-ray production, we calculate the electron spectral index  $\delta$  and the peak injected power  $P_{20}$  delivered by electrons with energies above a cutoff of 20 keV. Identifying the thick-target area with the total area of II $\alpha$  redshifts, we calculate the input heating flux  $F_{20} (= P_{20}/S_c)$  of electrons with energies above 20 keV.

### III. ANALYSIS

In order to obtain the pressure  $P_2$  in the evaporating region, we first determine the initial location of the evaporating plasma relative to the preflare transition region. For the case of collisional heating by thick-target electrons, the initial column depth of the flare transition region is given by solving for the depth  $N$  at which the collisional heating rate  $Q(N)$  just balances the transition region cooling rate  $R(N)$  (Canfield and Gunkler 1985).

For  $R$ , we adopt the optically thin cooling function (Raymond, Cox, and Smith 1976) expressed as

$$R(N) = f_5(P_0 + \mu m_H g N)/(1.1kT_{ch}),$$

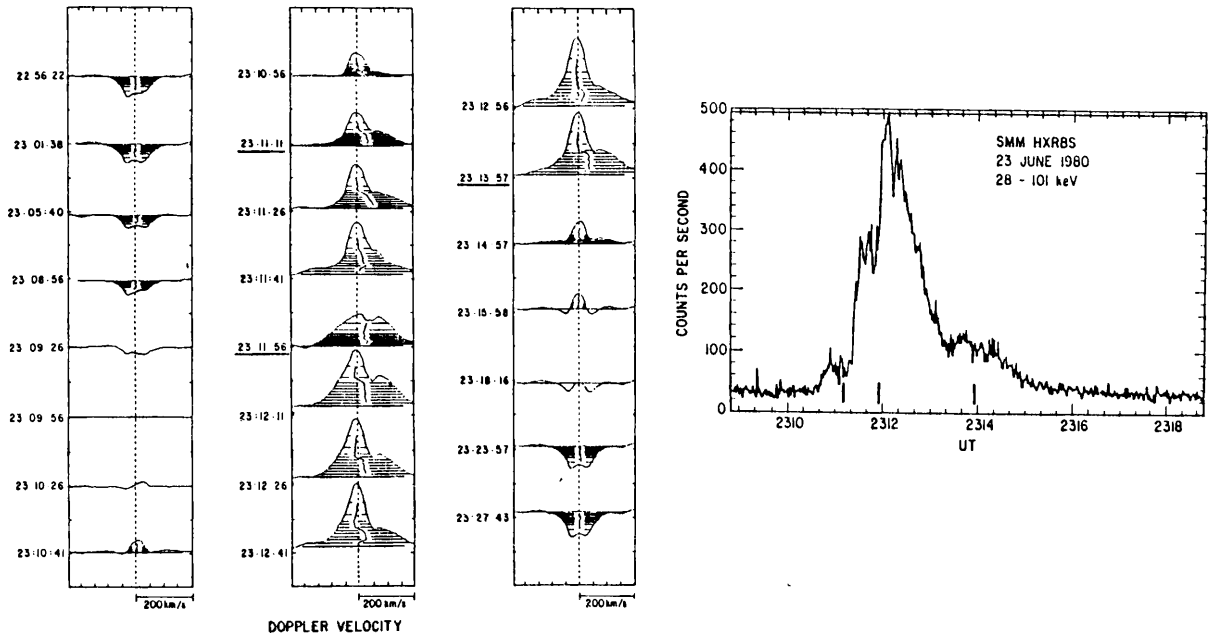


FIG. 1. – Comparison of SPO  $H\alpha$  (left panel) and HXRBS hard X-ray (right panel) observations of the 23 June 1980 flare. The temporal evolution of the  $H\alpha$  profile, (with the preflare absorption component subtracted) in a typical flaring pixel is shown. Note the pronounced red-wing emission during the periods of enhanced hard X-ray emission. This behavior is common to all five events and is interpreted as evidence for chromospheric downflows associated with each heating episode.

where  $\mu = 1.4$ ,  $f_5 = 7 \times 10^{-22}$  ergs  $\text{cm}^3 \text{s}^{-1}$  is the peak value of the radiative cooling function at  $T \approx 10^5$  K,  $P_0$  is the preflare coronal pressure, and  $T_{ch} (\approx 8000$  K) is the preflare chromospheric temperature. For  $Q$ , we adopt the smoothed thick-target heating function (Fisher, Canfield, and McClymont 1985) expressed as

$$Q(N) = \frac{\delta - 2}{6N_c} B\left(\frac{\delta}{2}, \frac{1}{3}\right) \alpha^{-\delta/2} \left[ a - b \left( \frac{N}{\alpha N_c} \right)^2 \right] F_c, \quad N < \alpha N_c \quad (3a)$$

$$Q(N) = \frac{\delta - 2}{6N_c} B\left(\frac{\delta}{2}, \frac{1}{3}\right) \left( \frac{N}{N_c} \right)^{-\delta/2} F_c, \quad N > \alpha N_c, \quad (3b)$$

where  $B(x, y)$  is the beta function,  $\delta$  is the electron spectral index,  $F_c$  is the injected flux of electrons with energies above a cutoff  $E_c$ , and  $N_c = 9.158 \times 10^{16} E_c^2$  is the electron stopping column depth. The normalization constants  $a$ ,  $b$ , and  $\alpha$  are chosen to ensure continuity of  $Q$  at the stopping depth.

Substituting parameters from Table 1, (using  $E_c \approx 20$  keV) we find that  $R \gg Q$  throughout the chromosphere of each flare, implying that the preflare chromosphere is sufficiently dense that it is able to radiate the excess heating of the electron beam without explosive chromospheric evaporation (Fisher 1987). Hence, the high-pressure region that drives evaporation (and the  $H\alpha$  downflows) is located initially above the transition region in the preflare corona that is heated by the beam. For the case of such thermal heating, Fisher (1987) has shown that the coronal pressure excess is given by

$$P_2 = P_0 (T_{f1}/T_0) + (4F^2 \rho_0/9)^{1/3}; \quad F = \int_0^{N_{tr}} Q dN,$$

where  $F$  is the heat flux deposited in the coronal portion of the loop,  $N_{tr} = n_0 L$  is the preflare transition region depth, and  $P_0$ ,  $T_0$ , and  $\rho_0$  denote preflare coronal pressure, temperature, and density, respectively. The quantity  $T_{fl}$  is the coronal flare temperature before significant evaporation has occurred and is computed by equating  $F$  to the Spitzer (1962) thermal conductivity flux.

Table 1 lists the derived values of  $N_{tr}$ ,  $F$ , and  $P_2$ . Setting  $P_1 = P_0 + \mu m_H g N_{tr}$  in equation (1), we compute  $v_d$  for each flare. For the 7 May, 23 June, and 24 June flares, the predicted and empirical velocities are consistent to within the observational uncertainties. For the 25 June flare – morphologically the most complex event – the observed velocity is approximately half the predicted value. For this extensive area flare, it is likely that the thick-target heat energy is distributed over a larger region than the observed H $\alpha$  redshift area  $S_c$ , which is subject to line-of-sight effects. Since  $v_d \sim P_2^{1/2} \sim F^{1/3}$ , a corresponding reduction in  $F_{20}$  will thereby reduce  $v_d$ . For the 30 April flare – an extremely compact event – the observed velocity is double the predicted value. In contrast to the previous case, we surmise that the flare energy is deposited over an area with small filling factor, such that the actual input heating flux is larger than  $F_{20}$ .

#### IV. CONCLUSIONS

We have shown that Fisher's (1987) relation predicts condensation downflow velocities that are consistent with observation to within a factor or two. This result indicates that the downflow velocity measured by H $\alpha$  redwing Doppler shifts can be used as a diagnostic of impulsive solar flare heating conditions. In particular, given a measure of the H $\alpha$  redshift, and an estimate of the preflare density, one can in principle invert this relation to compute the pressure excess driving chromospheric downflows and, thus, deduce the heating flux channeled into chromospheric evaporation.

In addition, our results demonstrate that the preflare coronal pressure is an important parameter that – in addition to the intensity of the heating flux – strongly influences the nature of chromospheric evaporation. The preflare coronal pressures in each flare are 2–3 orders of magnitude larger than characteristic coronal pressures in the quiet sun, and they exceed typical values ( $\sim 1$  dynes  $\text{cm}^{-2}$ ) adopted in hydrodynamic simulations of flares. These high pressures imply such large preflare chromospheric densities that the chromosphere is able to radiate excess flare heating without explosive chromospheric evaporation. Despite large input heating fluxes ( $F_{20} > 10^9$  ergs  $\text{cm}^{-2}$   $\text{s}^{-1}$ ), the consequent evaporation in each flare is sub-explosive with the high-pressure region that drives evaporation (and the observed H $\alpha$  downflows) being confined initially to the corona. Subsequent evaporation of the chromosphere is produced by thermal conduction from the hot flare corona. To date, this high preflare pressure case has not been modeled.

This work was supported by NASA contracts NAS5-28713 and NAS5-30431, and NSF grant AST-8615358

#### REFERENCES

- Acton, L.W., Canfield, R.C., Gunkler, T.A., Hudson, H.S., Kiplinger, A.L., and Leibacher 1982, *Ap.J.*, **263**, 409.  
 Canfield, R.C. and Gunkler, T.A. 1985, *Ap. J.*, **288**, 353.  
 Canfield, R.C., Zarro, D.M., Metcalf, T.R., and Lemen, J.R. 1988, *Ap. J.*, submitted.  
 Craig, I.J.D., McClymont, A.N., and Underwood, J.H. 1978, *Astr. Ap.*, **70**, 1.  
 Fisher, G.H. 1986, in *Lecture Notes in Physics*, Springer-Verlag, Vol. 255, p. 53.  
 Fisher, G.H. 1987, *Solar Phys.*, **113**, 307.  
 Fisher, G.H., Canfield, R.C., and McClymont, A.N. 1985, *Ap. J.*, **289**, 414.  
 Kundu, M.R., Schmahl, E.J., and Velusamy, T. 1982, *Ap. J.*, **253**, 963.  
 Raymond, J.C., Cox, D.P., and Smith, B.W. 1976, *Ap. J.*, **204**, 290.  
 Spitzer, L. 1962, in *Physics of Fully Ionized Gases*, Interscience, New York.  
 Zarro, D.M., Canfield, R.C., Strong, K.T., and Metcalf, T.R. 1988, *Ap. J.*, **324**, 582.